KSME

Springer

Journal of Mechanical Science and Technology 37 (9) 2023

Original Article
DOI 10.1007/s12206-023-0823-9

Keywords:
· Aerodynamic uplift force
· Drag and lift forces
· Pantograph
· High-speed train

Correspondence to:
Junsun Ahn
junsunahn@ut.ac.kr

Citation:
Kim, S. J., Kwon, H., Ahn, J. (2023). Aerodynamic performance of a pantograph cover for high-speed train. Journal of Mechanical Science and Technology 37 (9) (2023) 4681~4693.
http://doi.org/10.1007/s12206-023-0823-9

Received February 8th, 2023
Revised May 9th, 2023
Accepted June 7th, 2023

† Recommended by Editor
Han Seo Ko

Aerodynamic performance of a pantograph cover for high-speed train

Seung Joong Kim[1], Hyeokbin Kwon[2] and Junsun Ahn[3]

[1]Department of Mechanical Engineering, KAIST, 291 Daehak-ro, Yuseong-gu, Daejeon 34141, Korea, [2]Department of Transportation System Engineering, Korea National University of Transportation, 157 Cheoldobangmulgwan-ro, Uiwang-si, Gyeonggi-do 16106, Korea, [3]Department of Railway Vehicle System Engineering, Korea National University of Transportation, 157 Cheoldobangmulgwan-ro, Uiwang-si, Gyeonggi-do 16106, Korea

Abstract Three-dimensional unsteady turbulent flow around Faiveley CX pantograph was described by large-eddy simulations. The aerodynamic force distributions on the structures of the pantograph were explored comparing non-cover and cover cases against the incoming flow velocity of 200, 300, 400 km/h. The averaged drag and lift forces exerted on each component of the pantograph followed the second-order polynomial relations against the incoming flow velocity. The pantograph cover reduced the overall drag forces on the pantograph because the large recirculating zone with the strong negative pressure affected to the lower parts of the pantograph. In addition, when the pantograph cover was employed, the wall-normal direction of the lift force was changed from positive (uplift force) to negative (down force). By using the force and momentum balance considering all components of the pantograph, its aerodynamic uplift force was estimated, which was improved by including the specific forces around the knee joints, where the strong flow directly impinged. The pantograph cover reduced the mean and standard deviation values of the aerodynamic uplift forces as 40~48 % and 5~17 % compared to those for non-cover cases. Although more power was necessary to raise up the panhead to contact the catenary wire, it would help to improve the controller design to maintain the current collection performance by decreasing the uplift force fluctuations.

1. Introduction

High-speed train (HST), which runs by electrical energy at the speed of over 250 km/h, plays a major role in taking low carbon emissions [1]. It efficiently provides massive transfer of human and material resources between cities or continents, and contributes to reducing air pollution by relieving traffic congestion. To broaden these economic and environmental benefits, academia as well as industry has focused on increasing the maximum speed of the HST while maintaining high energy efficiency. To provide electrical energy to HST, pantographs contacting messenger wire (catenary) are installed at the roof of HST, which is called as the pantograph-catenary system. It is important for the pantograph to maintain proper contact force on the contact line by overcoming vibration transmitted from railway track, inertia force due to vehicle acceleration, crosswind effect, and unstable drag and lift force caused by external flow [2, 3]. Fig. 1 shows that in general, HST raises the rear pantograph mounted on the top roof of a body to collect an electric power through the contact wire while driving condition. The rear pantograph is strongly affected by an external flow of turbulent boundary layer, and the aerodynamic resistance of the pantograph system involves about 12 % of the total aerodynamic resistance [4]. To achieve high-speed conditions, the collection quality of the electric power should be supplied being stable, so it is necessary to stably maintain the contact force by the pantograph.

The contact force is composed of the aerodynamic uplift force by the pantograph and the controlling force by a passive or active feedback system. Since the controlling force is dependent on the aerodynamic uplift force by the pantograph, it is important to accurately estimate the aerodynamic uplift force in order to obtain the precise contact force. Pombo et al. [5] studied the

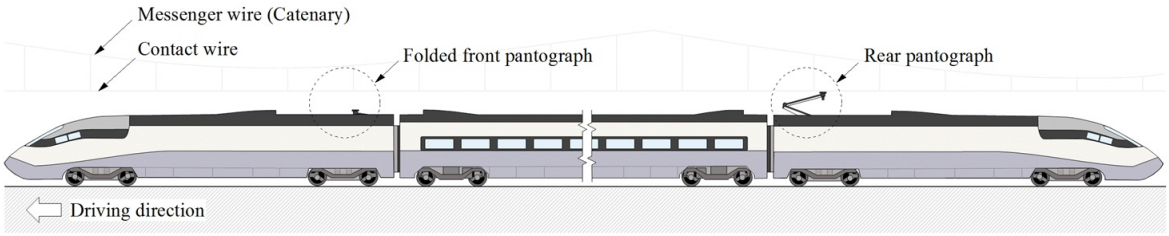

Fig. 1. Schematic diagram of a high-speed train.

aerodynamic uplift forces acting on the pantograph-catenary interaction using a co-simulation method between a finite element method and a detailed multi-body model. They found that the streamwise airflow under the train operating conditions contributed to uplifting the pantograph position and increased the contact force of the catenary system. This implies that a precise evaluation of aerodynamic uplift forces on the pantograph system is required to improve the electric power collection capability. Baker [6] proposed the calculating equation of the aerodynamic force acting on an entire train body surface, which considered the train speed and the fluctuating crosswind velocity. The proposed equation was simple and computationally economic, resulting in widespread usage to evaluate train stability and running characteristics.

Lee et al. [7] found that the fluctuations of the lift and drag forces on the pantograph system were related to the vortex shedding, and the modification of the panhead section shape significantly contributed to lessening the fluctuations than the modification of the upper arm geometry. Carnevale et al. [8] performed numerical simulations to evaluate the aerodynamic uplift force of the pantograph. They obtained the drag and lift forces on each component of single pantograph using the steady k-ω Reynolds averaged Navier-Stokes (RANS) equation, and these forces were applied to the virtual work principle to determine the aerodynamic uplift force. They emphasized that the aerodynamic uplift force was affected by not only the lift forces but the drag forces of each component, due to the kinematic linkage system of the pantograph. Song et al. [3] carried out the study of crosswind effects on the pantograph-catenary system of the HST by using the force and momentum balance in the linkage system of the pantograph. The lift and drag forces on each component of the pantograph were obtained using the computational fluid dynamics (CFD) method, and they were applied to force equilibrium equations assuming the pantograph to be a two-dimensional system to calculate the aerodynamic uplift force. The derived equations showed that the lift and drag forces were contributed to the aerodynamic uplift force according to the geometrical structure, such as the length and angle, of the pantograph. Kim et al. [9] adopted the method for the aerodynamic uplift force of the Faiveley CX pantograph to investigate the effects of the pantograph cover for 430 km/h. Three-dimensional unsteadiness flow nature is induced around HST, resulting in unsteady impulse forces on the body component [10]. To predict the accurate aerodynamic uplift force and its standard deviation, high fidelity turbulent model is required to capture the detailed flow field involved around the complex geometry of the pantograph.

In the present study, the lift and drag forces on the Faiveley CX pantograph, widely using in the railway system, were numerically investigated under the high-speed conditions as 200, 300, and 400 km/h. The pantograph cover, which installed for the purpose of electric apparatus protection with reducing drags, was included for the present numerical simulations, and the non-cover cases were also considered for comparison of the aerodynamic effects by the cover. The unsteady forces in time series were utilized to assess the aerodynamic uplift force by the improved derived analytical equation, which was considered all kinematic components and the geometrical characteristics of the pantograph.

To this aim, we carried out large eddy simulations (LESs) to explore turbulent flow around the pantograph (surrounded by the cover). This paper organized in four major sections. Sec. 2 describes the theoretical background and numerical methods, including boundary conditions and the grid generation method. Sec. 3 contains the results of the numerical simulations and the aerodynamic uplift force. Summary and conclusions are presented in Sec. 4. The grid resolution test and the detailed calculating procedure of the aerodynamic uplift force are listed in Appendix section.

2. Computational methodology

2.1 Numerical method

In the present study, we considered three incoming velocity conditions, U_0 = 200 (M = 0.16), 300 (M = 0.25), and 400 km/h (M = 0.33). The flow, in which Mach number (M) below 0.3, could be treated reasonably to be incompressible [11]. It is noted that the incoming velocity of 400 km/h should be considered to be compressible, but its disturbances by the compressible effect was very weak enough to be ignored [12-14]. The flows were, therefore, assumed to be incompressible for all numerical simulations. The governing equations of LES for the current incompressible turbulent flows are expressed as

$$\frac{\partial \overline{u}_i}{\partial x_i} = 0 , \tag{1}$$

$$\frac{\partial \overline{u}_i}{\partial t} + \frac{\partial \overline{u}_i \overline{u}_j}{\partial x_j} = -\frac{1}{\rho}\frac{\partial \overline{p}}{\partial x_i} + \frac{\partial \left(\sigma_{ij} - \tau_{ij}\right)}{\partial x_j} , \tag{2}$$

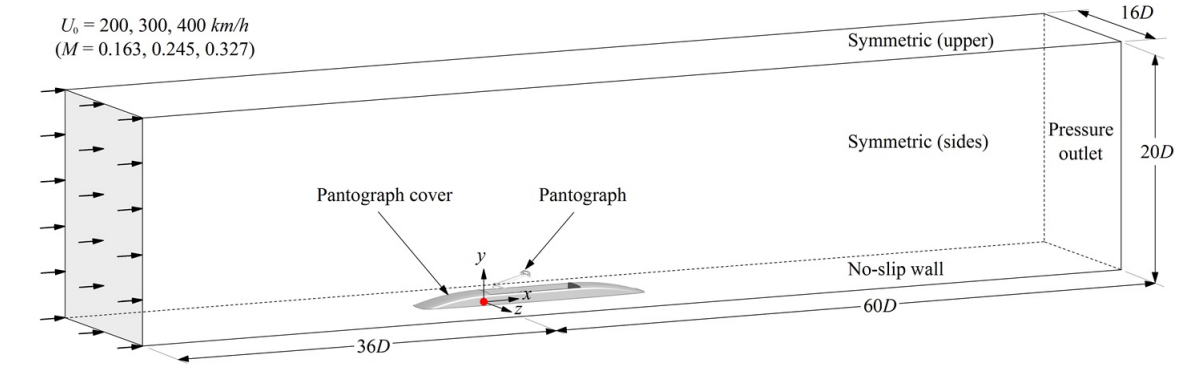

(a) Computational domain

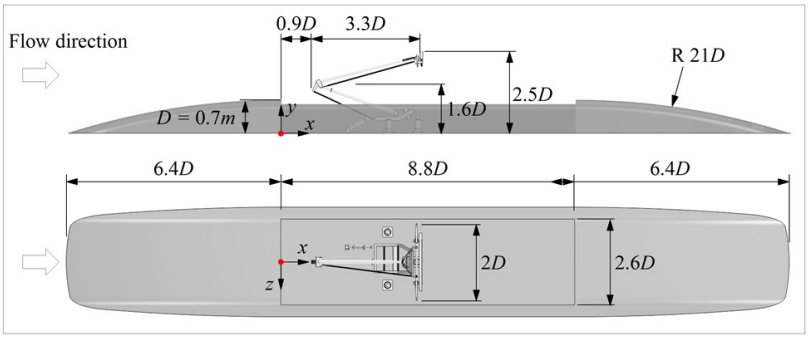

(b) Pantograph cover

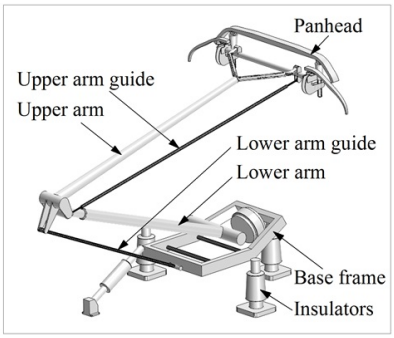

(c) Pantograph

Fig. 2. Schematic diagram of (a) the computational domain; (b) the pantograph cover; (c) Faiveley CX pantograph.

where u_i is the velocity component in x_i direction, p is the pressure, and ρ is the density. $\sigma_{ij} = \nu\left[\left(\partial\overline{u}_i/\partial x_j + \partial\overline{u}_j/\partial x_i\right) - 2/3\left(\partial\overline{u}_k/\partial x_k\right)\delta_{ij}\right]$ and $\tau_{ij} = \overline{u_i u_j} - \overline{u}_i\overline{u}_j$ are the viscosity stress tensor and the subgrid-scale (SGS) stress tensor. The over bars (⬚) on each physical quantity denote the space filtered variables by $G(x, x')$. The SGS stress tensor by the turbulent viscosity is resolved by the Smagorinsky model,

$$\nu_{SGS} = \left(C_S\Delta\right)^2\sqrt{2\overline{S}_{ij}\overline{S}_{ij}}\,, \tag{3}$$

where C_S is the Smagorinsky constant, Δ is the space filter (grid size) and $\overline{S}_{ij} = \left(\partial\overline{u}_i/\partial x_j + \partial\overline{u}_j/\partial x_i\right)/2$ is a strain-rate tensor. In this study, we adapted the dynamic Smagorinsky model [15], since the numerical simulation model expected a large velocity difference inside and outside of the cover. This subgrid scale model uses the dynamically determined C_S value in time and space, then, it can avoid the randomness of the general Smagorinsky subgrid model (fixed constant), i.e. the suitable C_S values can be employed by independent calculation on each cell location according to the flow field change in every time step. The numerical simulations were performed using the commercial CFD software *Star-CCM+*. For stability and accuracy of the numerical simulations with a complex flow geometry under the high-speed condition, the bounded central differencing scheme for the convection and the second order temporal discretization scheme were used and the wall-modeled LES (WMLES) technique, in which the flows near the wall surfaces were treated as the logarithmic law, were employed.

2.2 Flow geometry and boundary conditions

Fig. 2(a) shows a schematic diagram of the computational domain for the current numerical simulations. The domain size was fixed as (Lx, Ly, Lz) = (96D, 20D, 16D) for all simulations. The displayed dimensions were nondimensionalized by D, where D (= 0.7 m) is the depth of the pantograph cover as shown in Fig. 2(b). The origin point (0, 0, 0) was positioned at the bottom of the upstream surface on the cavity of the pantograph cover. Three different uniform velocities were 200, 300, and 400 km/h, and the corresponding Reynolds numbers based on the cover depth (D) were Re_D = 2.48×10^6, 3.72×10^6, and 4.96×10^6, respectively, where they were given at the inlet boundary condition located at x/D = −36. To overcome the convergence problem of numerical simulations, the initial incoming velocity was given 10 % of the target velocity and was increased as the step function of 25 %, 45 %, 70 %, and 100 % of the target velocity after each 0.05 sec. The target velocity was completely formed at 0.2 sec. The pressure outlet was employed at x/D = 60. The symmetric boundary conditions were used at the side surfaces (z/D = 8 and −8) and the top surface (y/D = 20). The no-slip conditions were employed at

the bottom surface (y/D = 0) including the pantograph cover and the pantograph surfaces. The detailed geometry and dimensions of the pantograph cover are displayed in Fig. 2(b). The cover shape was generated by the spheroidal shape in which radius of 21D with the smoothed trapezoid section profile. The exposed cover length to the streamwise direction was 21.6D. The rectangular cavity, 8.8D×D×2.6D, was positioned in the middle of the pantograph cover. The power collection posture was considered, and it was located inside the cavity with the position of the knee joint at (x/D, y/D, z/D) = (0.9, 1.6, 0). As shown in Fig. 2(c), the small, thin and complex components were simplified or ignored for the numerical simulations.

Fig. 3 shows the grid system for the numerical simulations for the cover cases. The current grid system was determined by the sensitivity test of the grid resolution. The detailed procedure and results are listed in Appendix A.1 section. The grid was generated with a hexa-type cell using the zonal embedded grid scheme [16] by dividing the computational domain into six refinement zones. Since the high pressure and velocity gradients were expected in the vicinity of the panhead and the knee region shown in the insets of Fig. 3. The minimum grid size was used here for 1.5 mm on the surfaces. Behind the regions, the grid size of 6 mm was adopted to describe the vortex shedding effect. The specific regions, including the pantograph, the upstream, and the downstream edges of the cavity (only for the cover case), were set to 12 mm. For resolving the turbulent boundary layer, 20 layers were used in the wall-normal direction by 1.1 growth rate within 10 mm. The maximum Δy+(non-dimensionalized wall-normal spacing by the viscous wall unit) was 31.4 for the non-cover case of 400 km/h and locally appeared at the knee point. For WMLES technique, to treat the near-wall turbulent flow according to the logarithmic law, the first wall-normal grid should be located at 10 < y+ < 100 [17, 18]. Therefore, the current grid resolution is sufficient to obtain reliable flow nature around the pantograph system under the high velocity condition. The total number of grids is 3.58×10^7 for the non-cover cases and 4.04×10^7 for the cover cases. A time step of $U_0\Delta t/D = 0.0119$ was employed in all simulations. The simulations were performed for $U_0t/D = 555.6$, and the flow data were sampled to obtain temporal averaged statistics and spectral analysis for the last 6700 time steps.

To verify the current numerical simulation setup, the spectral analysis of the wall pressure fluctuations at the center of the panhead contact strip was performed and compared with the previous study, as shown Fig. 4. Lee et al. [19] carried out the LES simulation of the full-scaled HST running an open-field at 300 km/h using the 3D compressible unsteady flows. Their data were compared with the current numerical simulation of the cover under 300 km/h case. The frequency range over 200 Hz, the current result showed the higher energy density due to the viscous damping of the compressible flow. The tonal peak frequencies were 195 Hz and 220 Hz, slightly different from each other. Since they considered all detailed geometries over the HST, the boundary layer over the roof was developed thick enough to submerge the rear pantograph due to flow disturbance on the surface. Oh et al. [20] reported that the incoming velocity magnitude near the height of the rear panhead was 87 % of the train running speed due to the developed boundary layer. The frequency of the pressure fluctuations is proportional to the incoming velocity; so, the present peak frequency is adjusted to 191.4 Hz (= 220 Hz×87 %), which is in good agreement with the previous study. It is concluded that the current numerical method and conditions are sufficient to describe the high-speed flow nature around the pantograph.

3. Results and discussion

3.1 Flow characteristics

In order to examine the flow characteristics around the pantograph system, three-dimensional vortical structures are described using the iso-surface of instantaneous Q-criterion colored by the velocity magnitude in Fig. 5. The vortical structures are developed long behind the pantograph components along the streamwise direction, and those become energetic and complex as the incoming velocity increases. At the knee joint, which connected part of the upper and lower arms, the highly unsteady flow arises since the incoming flow directly impinges without disturbances by surrounding components. The long-stretched wake flows are clearly observed behind the panhead. The incoming flow collides directly on the front side of the con-

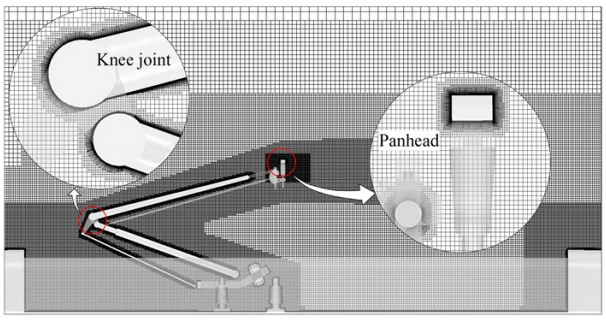

Fig. 3. Grid system for the cover case on the x-y plane at z = 0.

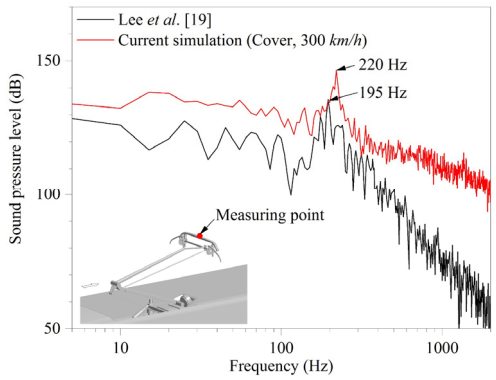

Fig. 4. Frequency spectra analysis at the center of the contact strip.

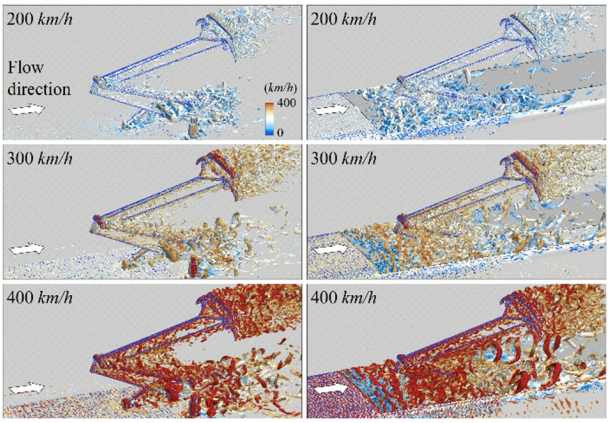

(a) Non-cover cases (b) Cover cases

Fig. 5. Instantaneous iso-surfaces of Q-criterion (Q = 1.5×10^{5}·/s^{2}) with velocity magnitude contour for (a) non-cover; (b) cover cases.

tact strip, where the section shape is square, and the flow is separated from the top and bottom edges.

The energetic unsteady flow motion, caused by a process of vortex shedding, occurs behind each component and is responsible for the fluctuating unsteady force of the pantograph system. For the non-cover cases, the boundary layer thickness before encountering the pantograph is 19, 16.1, and 13 mm for 200, 300, and 400 km/h, respectively. The base frame and insulators are exposed on the outer layer of incoming velocity, and the chaotic vortical structures are evolved due to their geometrical complexity. Meanwhile, for the cover cases, the incoming flow is separated at the upstream edge of the cavity and the periodical fluctuations are induced, which is called Kelvin-Helmholtz instability. The lower parts of the pantograph system such as the lower arm, lower arm guide and base frame are immersed in the unstable fluctuations inside the cavity region, so those of lift and drag forces are affected by the instability.

Fig. 6 shows the temporal averaged mean and root mean square (rms) velocity components of the non-cover and cover cases for 400 km/h on the x-y plane at z = 0. The results of the other velocities are not shown here because the contour shapes are similar for the incoming velocities. The streamwise mean velocity (U_x) contours are displayed in Fig. 6(a). For the non-cover case, three major stagnation points, marked by the white arrows, are formed in front of the panhead (1), the knee joint area (2), and the base frame (3). Behind these regions, the long-stretched flow structures are clearly observed due to the vortex shedding shown in Fig. 5. These flow in the downstream direction as parallel to the bottom surface without any disturbances to surrounding components. For the cover case, the large recirculating zone is generated below the pantograph by the flow separation from the upstream edge of the cavity. Due to the recirculating flow region, the stagnation point near the base frame is removed. Also, the wall-normal mean velocity (U_y) near the lower arm region (4), including the upper arm region, is strengthened in the negative direction, as shown in

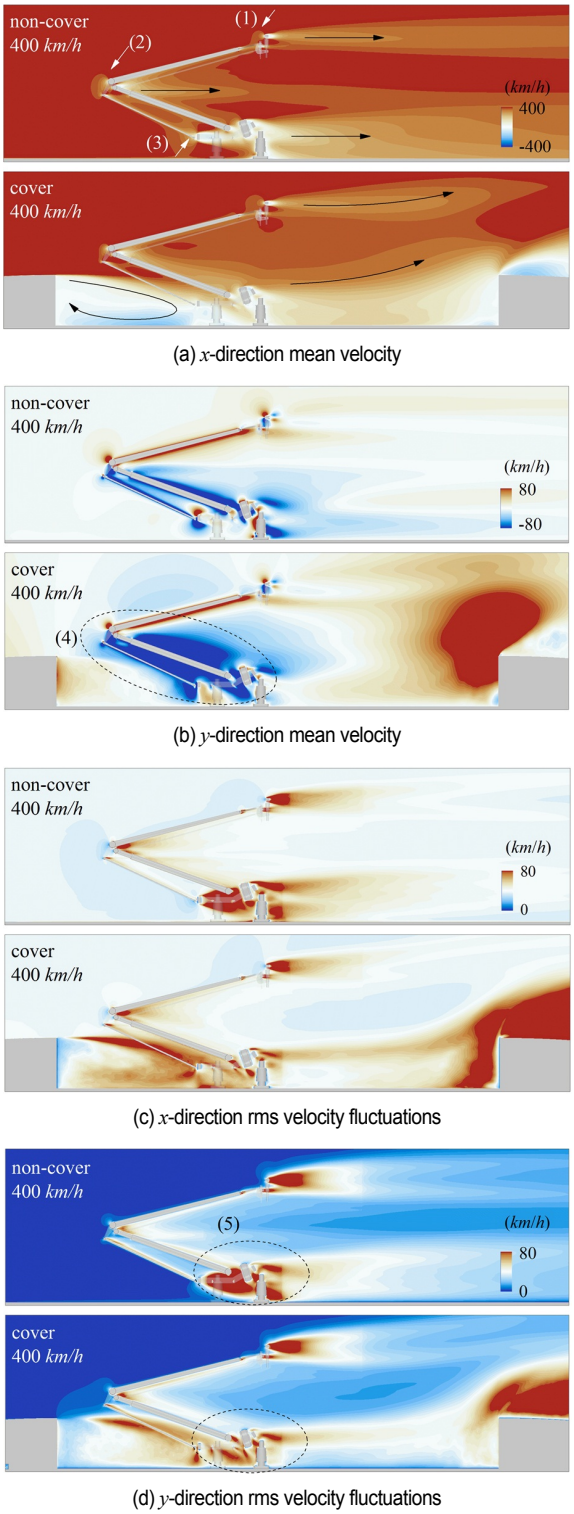

(a) x-direction mean velocity

(b) y-direction mean velocity

(c) x-direction rms velocity fluctuations

(d) y-direction rms velocity fluctuations

Fig. 6. Contours of the temporal averaged mean and rms velocity components on the x-y plane at z = 0 under 400 *km/h* condition.

Fig. 6(b). The rms velocity fluctuations to the streamwise and wall-normal directions are displayed in Figs. 6(c) and (d). The maximum locations coincide with those of the energetic wake flows shown in Fig. 5. For the cover case, the periodical insta-

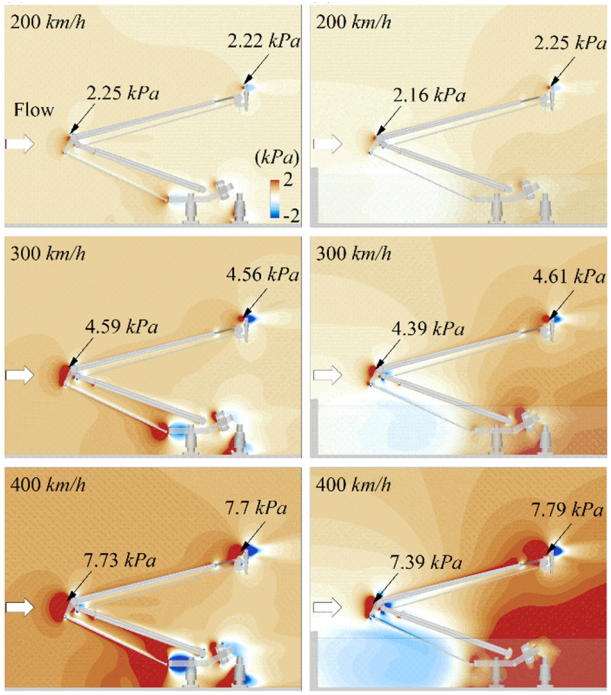

(a) Non-cover cases (b) Cover cases

Fig. 7. Contours of the temporal averaged mean pressure (*P*) on the *x*-*y* plane at *z* = 0 for (a) non-cover; (b) cover cases.

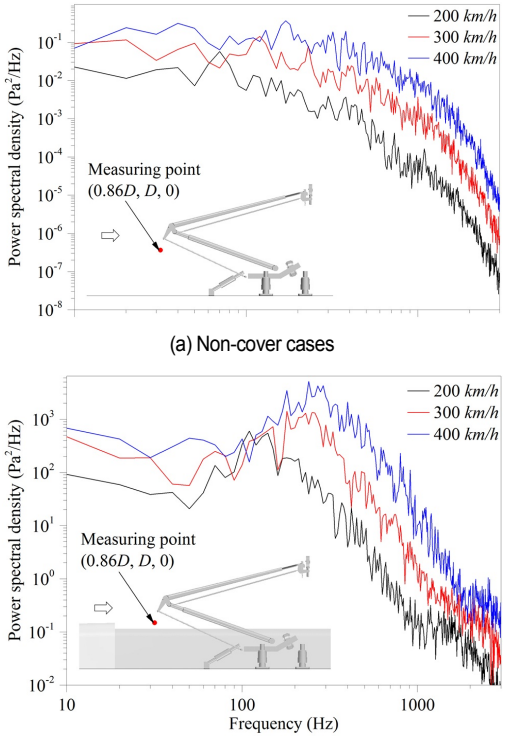

(a) Non-cover cases

(b) Cover cases

Fig. 8. Spectral analysis of the pressure fluctuations incoming flow before the pantograph for (a) non-cover; (b) cover cases.

bility flows which are separated from the upstream edge are collided on the lower arm and the lower arm guide, and the velocity fluctuations vicinity of the base frame (5) are weakened compared to the non-cover case.

Fig. 7 displays the temporal averaged mean pressure contour on the x-y plane at z = 0. The local maximum pressure occurs in front of the knee joint and the panhead area, and their values are measured at (1.0D, 1.5D, 0) and (4.1D, 2.4D, 0). For the non-cover cases, three local concentrating pressure areas correspond to the locations of the stagnation points. For the cover cases, the local maximum areas at the knee and the base frame are weakened due to the large negative pressure effect near the upstream edge by the recirculating flow; the maximum pressures around the knee region of the non-cover cases are approximately 4 % lower than those of the cover cases. The local negative pressure regions around the base frame disappears since the separated flows are dispersed until reattaching at the middle of the base frame and they are delayed inside the cavity as shown in Figs. 6(a) and (c). Meanwhile, the maximum pressure values around the panhead are slightly increased and those regions are expanded. As shown in Fig. 6(b), the incoming flow over the foreside cover is directed near the upper arm region to the cavity inside, and it causes to increase pressure near the upper arm and the panhead region. The indicated maximum pressure values are not proportional to the square of incoming velocity due to the flow interference effects of surrounding components, but those are satisfied as second-order polynomial relations (coefficient of determination, R^2 = 1) to the incoming velocity.

Fig. 8 shows the spectral analysis results of the pressure fluctuations for incoming flow before encountering the pantograph. The pressure fluctuations are measured at (0.86D, D, 0); this location represents well the characteristic of the Kelvin–Helmholtz instability for the cover cases. The power spectral densities for the non-cover cases are extremely lower than those for the cover cass at approximately 0.1 %, and the peak frequencies are not observed in the overall range. As mentioned above, since the boundary layer thickness of the incoming flow develops to approximately 20 mm (for the non-cover case under 400 km/h) before encountering the pantograph system, the mean flow without the velocity fluctuations (over the boundary layer) affects the components of the pantograph system. For cover cases, the shedding frequency is clearly observed due to the flow instability after the separation from the upstream edge of the cavity. The peak frequency of the pressure fluctuations as well as their energy density increases in proportion to the incoming velocity. It implies that the periodically oscillating flows, which have an energetic energy density, sustainably affect the knee joint part including the surrounding components.

The instantaneous wall pressure contours of the pantograph by the instability fluctuations separated from the upstream edge of the cavity are shown in Fig. 9. The high-pressure gradient from negative to positive arises at the panhead, the knee joint part, and the base frame, which correspond to the locations of the stagnation points as mentioned in Fig. 6(a). As

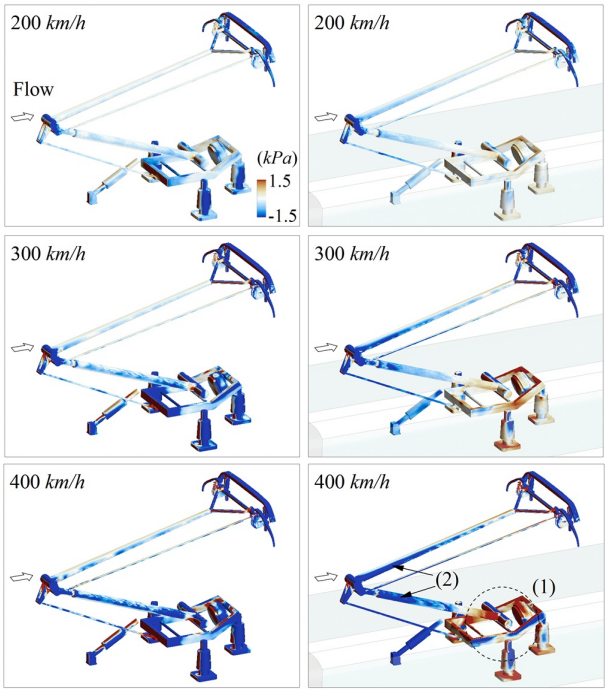

(a) Non-cover cases (b) Cover cases

Fig. 9. Contours of the instantaneous surface pressure on pantograph surface for (a) non-cover; (b) cover cases.

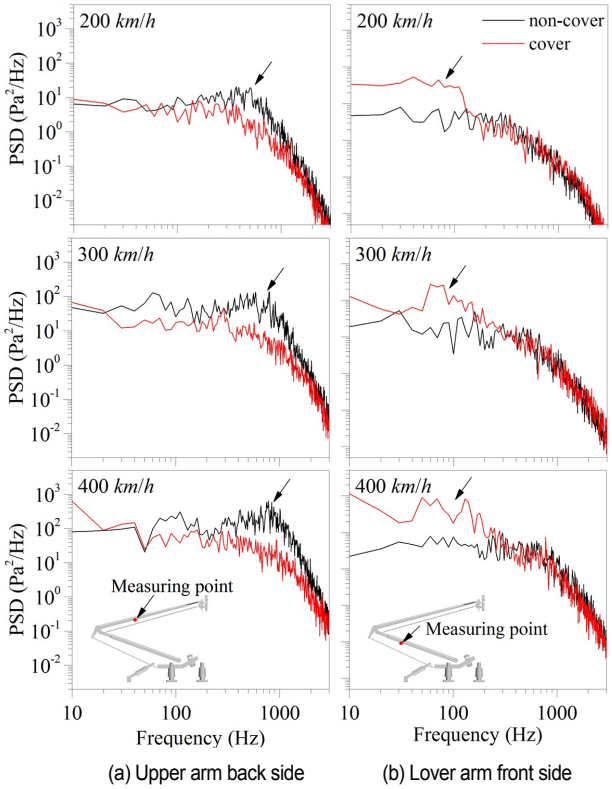

(a) Upper arm back side (b) Lover arm front side

Fig. 10. Spectral analysis of the wall pressure fluctuations on (a) upper arm back side; (b) lower arm front side.

increasing the incoming velocity, the strength of the pressure on the surfaces is also increased as the second-order polynomial relation, and the negative pressure regions are expanded. The contour shape and pressure level of the panhead and the knee joint are very similar between the cover and non-cover cases, whereas the negative and positive pressure regions of the base frame are decreased and increased, respectively, (1) for the cover cases due to the recirculating flow regime inside the cavity. The expanded negative pressure region (2) are clearly observed around the knee joint part for the cover cases. As shown in Fig. 6(b), the recirculating flow induces the mean stream flows to the cavity inside (i.e. it leads to a negative y direction), and this causes the expanded negative surface pressure region on the upper and lower arms. The pressure changes of the base frame do not affect to uplift force and the posture of the pantograph system, since the base frame is fixed on the top roof of the train. Also, the generated vortex structures from the panhead and the base frame shed behind the pantograph system do not affect the pressure distribution of surrounding components. This means that the pressure distribution of the cover cases around the knee joint area is the key cause of the changes in the aerodynamic uplift force.

Fig. 10(a) shows the spectral analysis results of the wall pressure fluctuations measured at the back side of the upper arm part (2.14D, 1.74D, 0). For the non-cover cases, the protruded peak frequency region from 500 to 800 Hz is revealed by the vortex shedding effect of the upper arm itself. The energy density and the peak frequency simultaneously increase as increasing the incoming velocity. For the cover cases, the characteristic frequency regions are reduced due to the changes in the flow regime near the knee joint part. Fig. 10(b) shows the spectral analysis results of the wall pressure fluctuations measured at the front side of the lower arm part (1.84D, 1.09D, 0). The power spectral densities of the non-cover and cover cases are relatively similar levels above 200 Hz for all velocity conditions. Meanwhile, the power spectral density levels for the cover cases within the frequency range of 200 Hz are stronger than those of the non-cover cases. The vortex shedding frequency generated by the separated flow from the upstream edge of the cavity directly influences the lower arm part, which is similar to the characteristic frequency peaks shown in Fig. 8(b). Sec. 3.1 concludes that the pantograph cover changes the flow regime and the velocity and pressure fields over the pantograph, and they act to increase or decrease the pressure fluctuations in the specific frequency range.

3.2 Force characteristics

Fig. 11 displays the temporal averaged drag forces for each component with the minimum and maximum values in regard to the incoming velocity. As shown in the pressure distribution of Fig. 7, the minimums and maximums values as well as the drag forces are also satisfied with the second-order polynomial relation to the incoming velocity. The pantograph cover plays a role to decrease the averaged drag forces for the lower arm, the lower arm guide, and the base frame by approximately

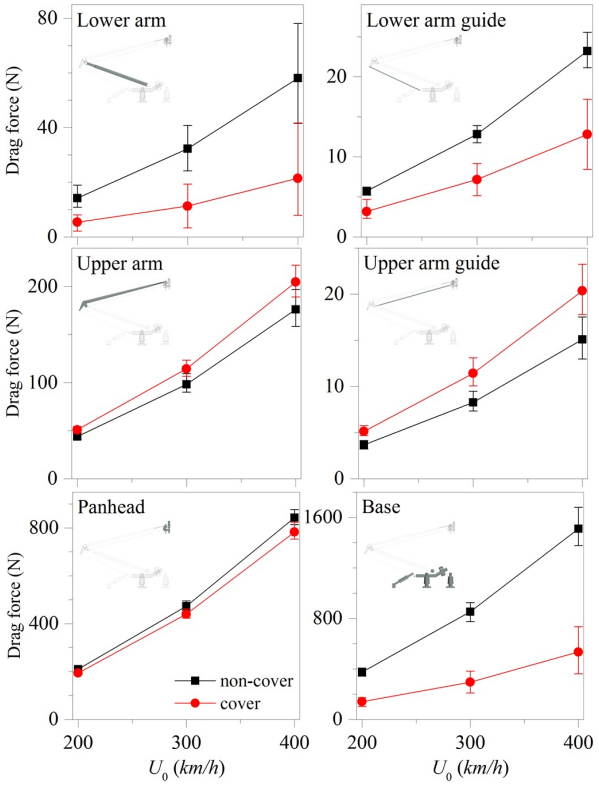

Fig. 11. Temporal averaged drag forces for each component with the minimum and maximum values.

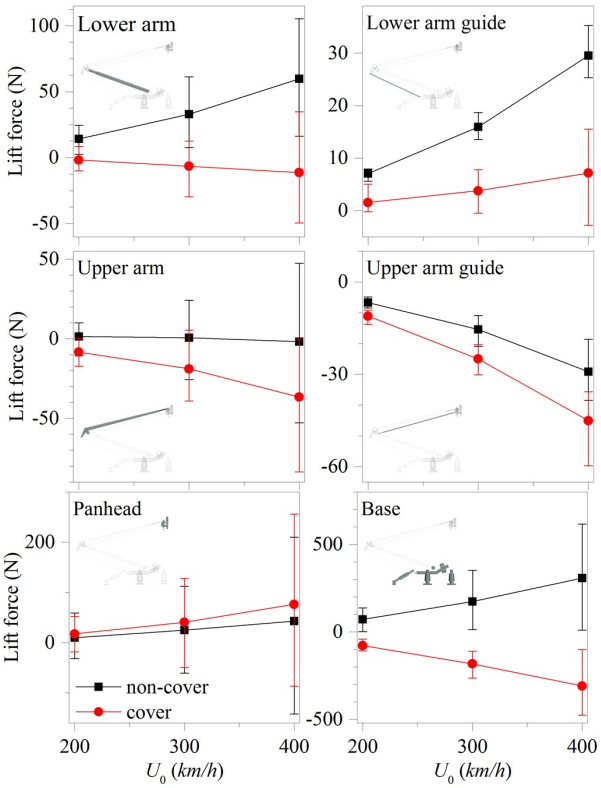

Fig. 12. Temporal averaged lift forces for each component with the minimum and maximum values.

63 %, 44 %, and 64 %, respectively. As shown in the previous chapter, the lower arm and the lower arm guide are partially immersed in the negative pressure region generated by the recirculating flow, and the base frame is influenced by the reconstructed flow after the reattachment to the wall not the mean flow over the boundary layer. Those mainly cause the large drag reduction for the components. The downward flow inside the cavity region shown in Fig. 6(b) contributes to increasing drag force on the upper arm and the upper arm guide by approximately 16 % and 38 % due to the pantograph posture. The high-pressure region of the cover cases, occurring behind the pantograph by the downstream face of the cavity reduces the pressure difference around the panhead as shown in Fig. 7, and it results in 7 % drag reduction.

Fig. 12 shows the temporal averaged lift forces for each component with the minimum and maximum values in regard to the incoming velocity. The pantograph cover increases the down force (i.e. the negative lift force) for all components except the panhead. In particular, the lower arm and the base frame, largely affected by the negative pressure region of the recirculating flow, change the y-direction of the forces from positive (lift force) to negative (down force). The linkage posture of the pantograph makes the down forces act on the upper arm and the upper arm guide by the mean flow. This becomes more significant for the cover cases due to the widened negative y-direction velocity region shown in Fig. 6(b), contributing to the additional down force. The lift force of the panhead increases approximately 7 % due to the alleviated high-pressure region below the panhead. Regardless of the cover existence, for all components, the differences between the minimum and maximum of the lift force are more than twice as large as those of the drag force, and especially that of the panhead is more than five times larger.

Fig. 13 shows the time series data of total drag and lift forces acting on the pantograph by arithmetically summing the time series force data of each component excluding the pantograph cover. The time-averaged forces of the pantograph are summarized in Table 1, and the forces including the cover effect are also listed for comparison. The pantograph cover gives the effects of reducing the total drag and lift forces for the pantograph.

For the drag force of the cover cases, the averaged values are decreased by approximately 41 %, while the degrees of the drag force fluctuations are similar to those of the non-cover cases. The lift force occurs for the non-cover cases, but it changes to the down force by applying the pantograph cover. In addition, the degrees of the lift force fluctuations are significantly decreased as approximately 50 % compared to the non-cover cases. The drag and lift forces are, however, largely increased to 2.3 times and 21 times when the forces of the pantograph cover are included as shown in Table 1. The exposed area of the pantograph cover is wider and longer than the entire surface area of the pantograph system, so the forces strongly occur under a similar pressure environment. Moreover,

Table 1. Temporal averaged total drag and lift forces.

	Non-cover		Cover			
			Pantograph		Pantograph + cover	
Speed (km/h)	Drag (N)	Lift (N)	Drag (N)	Lift (N)	Drag (N)	Lift (N)
200	651.0	97.4	400.0	-79.8	2123.4	2240.3
300	1477.7	232.6	879.1	-188.2	4884.0	5057.5
400	2626.6	409.3	1576.4	-318.2	8611.4	8935.7

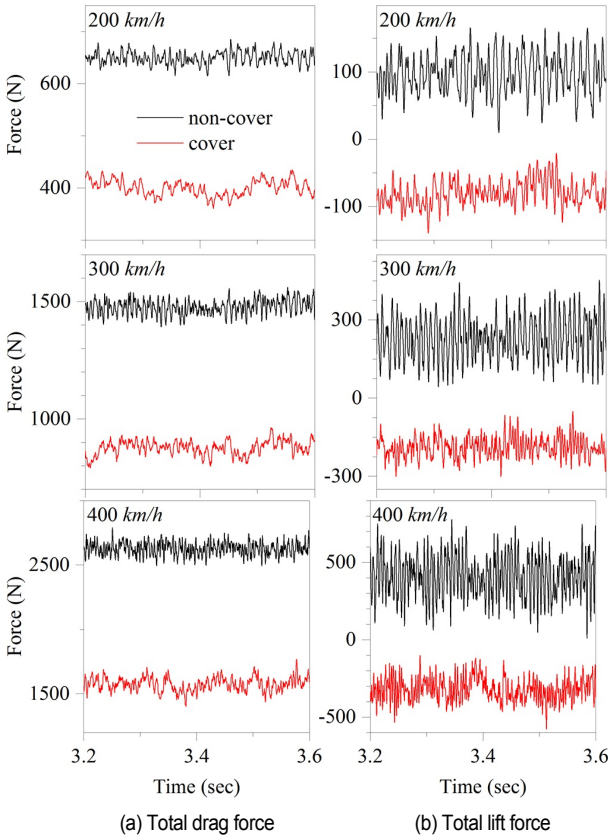

Fig. 13. (a) Total drag; (b) total lift forces acting on the pantograph.

the downstream face of the cavity gives additional drag force by the collision of the reconstructed flow regime, and near the upstream face and downstream edge of the cavity, the negative pressure regions by the recirculating flow increases the lift force. It is noted that although the forces on the base frame and the cover highly occupy to the total drag and lift forces, those forces do not influence the posture of the pantograph system since they are fixed on the top roof of HST.

3.3 Aerodynamic uplift force

Fig. 14 shows two-dimensional schematic diagram of the pantograph system and the force distribution on each component for the force transmission path from the lower arm to the panhead. The aerodynamic uplift force (F_{uplift}) of the pantograph

Table 2. Specified drag and lift forces for the upper arm part.

Speed (km/h)	Force (N)	Non-cover			Cover		
		BG	GI	GK	BG	GI	GK
200	Drag	20.1	17.3	6.5	22.3	20.7	7.9
	Lift	-11.0	16.1	-3.6	-20.8	17.6	-5.1
300	Drag	44.5	39.0	14.8	50.2	46.4	17.8
	Lift	-27.7	36.4	-8.1	-46.6	39.3	-11.6
400	Drag	79.3	70.5	26.4	91.1	81.9	31.7
	Lift	-52.2	64.8	-14.5	-84.2	68.3	-20.7

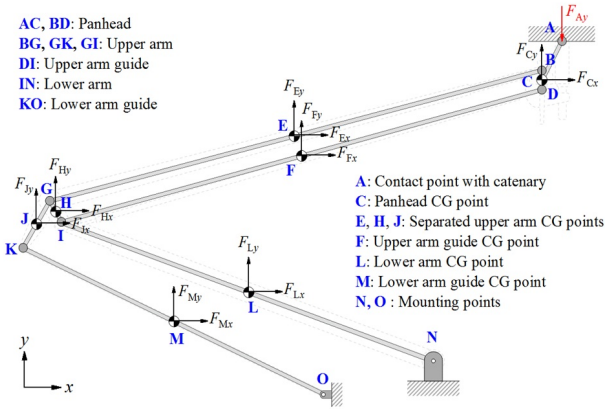

Fig. 14. Schematic diagram of the pantograph system for calculating aerodynamic uplift force.

system can be substituted into the reaction force (F_{Ay}) at the contact point between the panhead and the catenary. To this aim, all components including the catenary wire are assumed to be a two-dimensional rigid body and a stationary system. The forces on z-direction are not considered due to no effect on the pantograph motion, and the deformation and vibration of the component itself are ignored. The surface force on each component are imposed at the center of gravity (CG) point as a concentrated force.

The aerodynamic uplift force is derived using the force and momentum equilibrium equation. Song et al. [3] proposed the calculation method for the aerodynamic uplift force, but the forces on the lower arm guide and the upper arm guide were excluded from their equation. However, those of the drag and lift forces are not small enough to negligible under the high-speed velocity condition, as shown in Figs. 11 and 12. Furthermore, as shown in Fig. 9, the upper arm forces should be carefully measured because the knee joint part (GK and GI) of the upper arm expose to high-pressure region and its moment acts in an opposite direction of the upper arm body (BG). Table 2 shows that the drag and lift forces at the small parts of GK and GI near the knee joint are comparable to those of BG. Especially, the direction of the lift forces for GI is opposite to that of BG and GK. In this study, it is necessary to improve the derived equation for the aerodynamic uplift force by considering all components as well as the detailed upper arm compo-

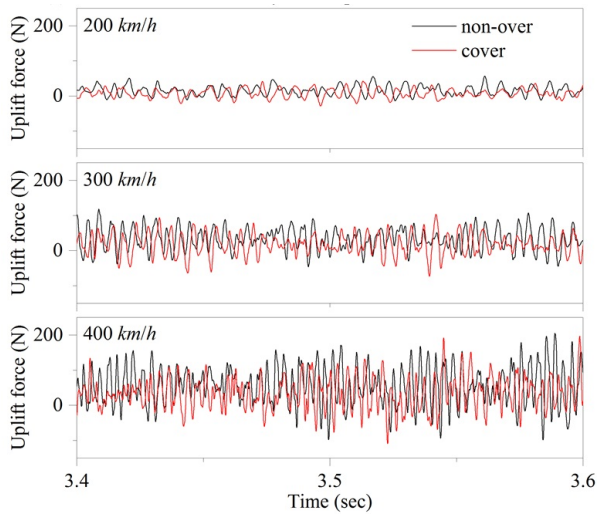

(a) Time series data of aerodynamic uplift force

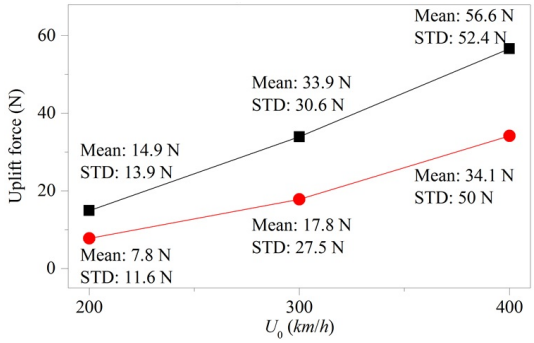

(b) Mean of aerodynamic uplift force

Fig. 15. (a) Time series data; (b) mean and standard deviation values of aerodynamic uplift force.

nents for CX pantograph as follows:

$$\begin{aligned} F_{uplift} = F_{Ay} = {} & 0.004F_{Cx} + 0.977F_{Cy} + 0.064F_{Ex} \\ & + 0.701F_{Ey} + 0.086F_{Fx} + 0.708F_{Fy} \\ & + 0.146F_{Hx} + 0.432F_{Hy} + 0.16F_{Jx} \\ & + 0.41F_{Jy} + 0.079F_{Lx} + 0.219F_{Ly} \\ & + 0.093F_{Mx} + 0.198F_{My}. \end{aligned} \quad (4)$$

The constants in which multiplied to the force variables are calculated by the geometry characteristics such as lengths and angles of each component, and its detailed procedure is shown in the Appendix A.2 section. As shown in Eq. (4), we confirm that not only the lift forces (20~98 %) but also the drag force (0.4~16 %) on each component contribute to the aerodynamic uplift force. In particular, the contribution of the panhead lift force (F_{Cy}) (97.7 %) is higher than that of the other forces, implying that the panhead lift force has the greatest effect on the aerodynamic uplift force.

Fig. 15(a) shows the time series data of the evaluated aerodynamic uplift force by applying the time history of the drag and lift forces on each component into Eq. (4). As the same with the previous results, the fluctuation magnitude of the aerodynamic uplift force is expanded as increasing the incoming velocity. The force differences between the minimums and maximums for the cover cases are quantitatively reduced compared to those for the non-cover cases. Fig. 15(b) shows the mean and standard deviation values of the aerodynamic uplift force. The mean values are satisfied with the second-order polynomial relation in terms of the incoming velocity as the coefficient of determination of R^2 = 0.999; $F_{uplift} = 0.0003U_0^2 + 0.0131U_0$ for the non-cover cases, and $F_{uplift} = 0.0002U_0^2 - 0.0109U_0$ for the cover cases. The mean forces and its standard deviations for cover cases are decreased as 40~48 % and 5~17 % compared to those for the non-cover cases. The pantograph cover has the drawback of decreasing the magnitude of the aerodynamic uplift force, but gives an advantage for relieving its fluctuation. Therefore, the pantograph cover can be contributed to improving the electric power collection capability by decreasing the unsteadiness of the pantograph posture under a high-speed environment.

4. Conclusions

Large-eddy simulations were performed to describe three-dimensional unsteady turbulent flow around Faiveley CX pantograph under the high-speed condition of 200, 300 and 400 km/h, to investigate the effects of non-cover and cover surrounding the pantograph. For the non-cover cases, the mean flow over the turbulent boundary layer directly met the pantograph system; however, for the cover cases, the flow instability occurred at the leading edge of the cavity, and the large recirculating zone with the negative pressure and the reattachment affect to the pantograph system. The drag and lift forces were obtained for each component of the pantograph, and their averaged mean values were grown with the second-order polynomial relation. The cover reduced the overall drag for the pantograph, however the direction of the lift force was changed from positive (uplift force) to negative (down force). To estimate the aerodynamic uplift force of the pantograph, the pantograph system was modeled using the force and momentum balance considering all the component of the pantograph. It was found that the aerodynamic uplift forces were satisfied with the second-order polynomial relation against the incoming velocity. The cover made that the mean and standard deviation values of the aerodynamic uplift forces were decreased as 40~48 % and 5~17 % compared to those for the non-cover cases. This represented that although the pantograph cover seemed to reduce the current collection performance by reducing the mean values of the aerodynamic uplift force, it can help the controller design to improve the performance by relieving the unsteadiness of the flow.

Acknowledgments

This study was supported by a grant from the National Research Foundation of Korea (No. 2020R1G1A1003512) and

Korea National University of Transportation Industry-Academy Cooperation Foundation in 2021.

Nomenclature

CG : Center of gravity
C_S : Smagorinsky constant
D : Depth of the pantograph cover
F_{Ay} : Reaction force at the contact point between the panhead and the catenary
F_{uplift} : Aerodynamic uplift force of the pantograph system
$G(x,x')$: Space filter
HST : High-speed train
k : Turbulent kinetic energy
LES : Large-eddy simulation
Lx : Streamwise domain length
Ly : Wall-normal domain length
Lz : Spanwise domain length
M : Mach number
p : Pressure
rms : Root mean square
SGS : Subgrid-scale
S_{ij} : Strain-rate tensor
STD : Standard deviation
t : Time
Δt : Time step
U_0 : Uniform incoming velocity
U_x : Streamwise mean velocity
U_y : Wall-normal mean velocity
u_i : Velocity components according to the directions in the cartesian coordinate
$WMLES$: Wall-modeled LES
x_i : Directions in the cartesian coordinate
x : Streamwise direction
y : Wall-normal direction
$\Delta y+$: Non-dimensionalized wall-normal spacing by the viscous wall unit
z : Spanwise direction
Δ : Space filter (grid size)
v : Kinematic viscosity of fluid
v_{SGS} : SGS stress tensor by the turbulent viscosity
ρ : Density of fluid
σ_{ij} : Viscosity stress tensor
τ_{ij} : Subgrid-scale stress tensor
ω : Turbulent dissipation rate

References

[1] Z. Chen, M. Jiang, L. Qi, W. Wei, Z. Yu, W. Wei, X. Yu and J. Yan, Using existing infrastructures of high-speed railways for photovoltaic electricity generation, *Resources, Conservation and Recycling*, 178 (2022) 106091.

[2] Y. Song, Z. Wang, Z. Liu and R. Wang, A spatial coupling model to study dynamic performance of pantograph-catenary with vehicle-track excitation, *Mechanical Systems Signal Process*, 151 (2021) 107336.

[3] Y. Song, F. Duan, S. Gao, F. Wu and Z. Liu, Crosswind effects on current collection quality of railway pantograph-catenary: a case study in Chengdu-Chongqing passenger special line, *IEEE Transactions on Instrumentation and Measurement*, 71 (2022) 1-13.

[4] Z. Dai, T. Li, N. Zhou, J. Zhang and W. Zhang, Numerical simulation and optimization of aerodynamic uplift force of a high-speed train, *Railway Engineering Science*, 30 (1) (2022) 117-128.

[5] J. Pombo, J. Ambrósio, M. Pereira, F. Rauter, A. Collina and A. Facchiinetti, Influence of the aerodynamic forces on the pantograph-catenary system for high-speed trains, *Vehicle System Dynamics*, 47 (11) (2009) 1327-1347.

[6] C. J. Baker, The simulation of unsteady aerodynamic cross wind forces on trains, *Journal of Wind Engineering and Industrial Aerodynamics*, 98 (2010) 88-99.

[7] Y. Lee, J. Rho, T. K. Kim, D. H. Lee and H. B. Kwon, Experimental studies on the aerodynamic characteristics of a pantograph suitable for a high-speed train, *Journal of Rail and Rapid Transit*, 229 (2) (2015) 136-149.

[8] M. Carnevale, A. Facchinetti and D. Rocchi, Procedure to assess the role of railway pantograph components in generating the aerodynamic uplift, *Journal of Wind Engineering and Industrial Aerodynamics*, 160 (2017) 16-29.

[9] S. J. Kim, H. Kwon and J. Ahn, Numerical analysis of pantograph for aerodynamic uplift force, *Journal of the Korea Society for Railway*, 25 (7) (2022) 510-519.

[10] H. Choi, J. Lee and H. Park, Aerodynamics of heavy vehicle, *Annual Review of Fluid Mechanics*, 46 (2014) 441-468.

[11] J. D. Anderson, *Fundamentals of Aerodynamics*, Fifth Eds., McGraw-Hill (2010).

[12] Y. J. Moon, H. Oh and J. Seo, Aerodynamic investigation of three-dimensional wings in ground effect for aero-levitation electric vehicle, *Aerospace Science and Technology*, 9 (6) (2005) 485-494.

[13] S. Ding, Q. Li, A. Tian, J. Du and J. Liu, Aerodynamic design on high-speed trains, *Acta Mechanica Sinica*, 32 (2016) 215-232.

[14] Y. Zhao, Z. Yang, Q. Li and C. Xia, Analysis of the near-field and far-field sound pressure generated by high-speed trains pantograph system, *Applied Acoustics*, 169 (2020) 107506.

[15] M. Germano, U. Piomelli, P. Moin and H. Carbot, A dynamic subgrid-scale eddy-viscosity model, *Physics of Fluids*, 3 (7) (1991) 1760-1765.

[16] A. G. Kravcheko, P. Moin and R. Moster, Zonal embedded grid for numerical simulations of wall-bounded turbulent flows, *Journal of Computational Physics*, 127 (1996) 412-423.

[17] S. T. Bose and G. I. Park, Wall-modeled large-eddy simulation for complex turbulent flows, *Annual Review of Fluid Mechanics*, 50 (2018) 536-561.

[18] H. Choi and P. Moin, Grid-point requirements for large eddy simulation: chapman's estimates revisited, *Physics of Fluids*, 24 (2012) 011702.

[19] S. Lee, C. Cheong, B. Kim and J. Kim, Comparative analysis of surface pressure fluctuations of high-speed train running in

open-field and tunnel using LES and wavenumber-frequency analysis, *Applied Sciences*, 11 (2021) 11702.

[20] H. K. Oh, H. Kwon, M. Kwak, S. Kim and C. Park, Measurement and analysis for the upper side flow boundary layer of a high speed train using wind tunnel experiments with a scaled model, *Journal of the Korea Society for Railway*, 19 (1) (2016) 11-19.

Appendix

A.1 Grid resolution test

To assess the sensitivity of the grid resolution, several trial calculations were carried out for the cover case for 400 km/h.

Table A.1. The drag and lift forces by the grid resolution.

	Drag force (N)			Lift force (N)		
	Coarse	**Current**	Fine	Coarse	**Current**	Fine
Lower arm	26.0	**21.5**	19.7	-16.5	**-11.3**	-12.5
Lower arm guide	12.7	**12.8**	12.8	7.4	**7.1**	6.8
Upper arm (BG)	88.6	**91.1**	91.0	-107.3	**-84.2**	-86.3
Upper arm (GI)	81.2	**81.9**	83.1	68.6	**68.3**	64.9
Upper arm (GK)	31.6	**31.7**	32.3	-20.3	**-20.7**	-21.2
Upper arm guide	20.7	**20.4**	20.6	-45.8	**-45.0**	-45.8
Panhead	780.3	**783.2**	766.1	59.4	**76.3**	72.7
Base frame	536.8	**533.8**	555.2	-314.6	**-308.7**	-290.6
Sum	1577.9	**1576.4**	1580.7	-369.0	**-318.2**	-312.0

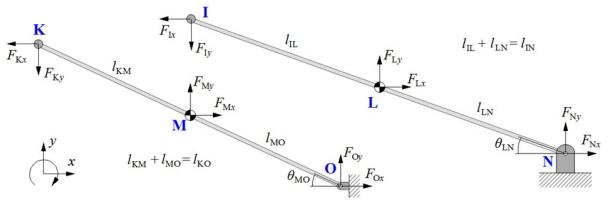

(a) Lower arm guide (b) Lower arm

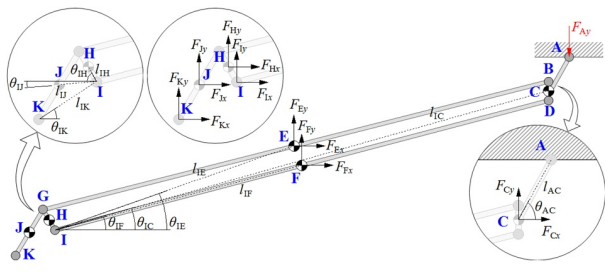

(c) Upper arm, upper arm guide and panhead

Fig. A.1. Schematic diagram of three major components of the pantograph.

We compared the drag and lift forces acting on each component since the purpose of current numerical simulations was to obtain the aerodynamic uplift force. Table A.1 shows the temporal averaged drag and lift forces for three grid cases: coarse grid (2.89×10^7), current grid (4.04×10^7), and fine grid (6.16×10^7). The force results of the current grid resolution are comparatively in good agreement with those for fine grid resolution. The lower arm results show approximately 9 % difference but those force values are acceptable, since their absolute values of difference only 1-2 N. It is, therefore, concluded that the current numerical method and conditions are sufficient to describe the high-speed flow nature around the pantograph.

A.2 Derivation of aerodynamic uplift force

Fig. A.1 shows the schematic diagram of three major components for calculating the aerodynamic uplift force. Here, $F_{\alpha\beta}$ is the force at α point to the β-direction, and $l_{\gamma\delta}$ is the length from point γ to point δ, and $\theta_{\varepsilon\zeta}$ is the angle between the component εζ and horizontal line (x-axis). The derived procedure for the aerodynamic uplift force is listed below.

From the lower arm guide diagram of Fig. A.1(a)

$$\sum F_x = -F_{Kx} + F_{Mx} + F_{Ox} = 0 \tag{A.1}$$

$$\sum F_y = -F_{Ky} + F_{My} + F_{Oy} = 0 \tag{A.2}$$

$$\sum M_K = -F_{Mx}\left(l_{KM}\sin\theta_{MO}\right) - F_{My}\left(l_{KM}\cos\theta_{MO}\right) - F_{Ox}\left(l_{KO}\sin\theta_{MO}\right) - F_{Oy}\left(l_{KO}\cos\theta_{MO}\right) = 0. \tag{A.3}$$

From the lower arm diagram of Fig. A.1(b)

$$\sum F_x = -F_{Ix} + F_{Lx} + F_{Nx} = 0 \tag{A.4}$$

$$\sum F_y = -F_{Iy} + F_{Ly} + F_{Ny} = 0 \tag{A.5}$$

$$\sum M_I = -F_{Lx}\left(l_{IL}\sin\theta_{LN}\right) - F_{Ly}\left(l_{IL}\cos\theta_{LN}\right) - F_{Nx}\left(l_{IN}\sin\theta_{LN}\right) - F_{Ny}\left(l_{IN}\cos\theta_{LN}\right) = 0. \tag{A.6}$$

From the upper arm, upper arm guide, and pantograph diagram of Fig. A.1(c)

$$\sum F_x = F_{Cx} + F_{Ex} + F_{Fx} + F_{Hx} + F_{Ix} + F_{Jx} + F_{Kx} = 0 \tag{A.7}$$

$$\sum F_y = -F_{Ay} + F_{Cy} + F_{Ey} + F_{Fy} + F_{Hy} + F_{Iy} + F_{Jy} + F_{Ky} = 0 \tag{A.8}$$

$$\begin{aligned}\sum M_I = {} & F_{Ay}\left(l_{AC}\cos\theta_{AC} + l_{IC}\cos\theta_{IC}\right) + F_{Cx}\left(l_{IC}\sin\theta_{IC}\right) \\ & - F_{Cy}\left(l_{IC}\cos\theta_{IC}\right) + F_{Ex}\left(l_{IE}\sin\theta_{IE}\right) - F_{Ey}\left(l_{IE}\cos\theta_{IE}\right) \\ & + F_{Fx}\left(l_{IF}\sin\theta_{IF}\right) - F_{Fy}\left(l_{IF}\cos\theta_{IF}\right) + F_{Hx}\left(l_{IH}\sin\theta_{IH}\right) \\ & + F_{Hy}\left(l_{IH}\cos\theta_{IH}\right) - F_{Jx}\left(l_{IJ}\sin\theta_{IJ}\right) + F_{Jy}\left(l_{IJ}\cos\theta_{IJ}\right) \\ & - F_{Kx}\left(l_{IK}\sin\theta_{IK}\right) + F_{Ky}\left(l_{IK}\cos\theta_{IK}\right) = 0.\end{aligned} \tag{A.9}$$

Put Eq. (A.1)$\times\sin\theta_{MO}$ and Eq. (A.2) $\times\cos\theta_{MO}$ into Eq. (A.3)

$$F_{Ky} = -F_{Kx}\frac{\sin\theta_{MO}}{\cos\theta_{MO}} + F_{Mx}\frac{l_{MO}}{l_{KO}}\frac{\sin\theta_{MO}}{\cos\theta_{MO}} + F_{My}\frac{l_{MO}}{l_{KO}}. \quad \text{(A.3′)}$$

Put Eq. (A.4)$\times\sin\theta_{LN}$ and Eq. (A.5) $\times\cos\theta_{LN}$ into Eq. (A.6)

$$F_{Ix}\sin\theta_{LN} + F_{Iy}\cos\theta_{LN} = F_{Lx}\frac{l_{LN}}{l_{IN}}\sin\theta_{LN} + F_{Ly}\frac{l_{LN}}{l_{IN}}\cos\theta_{LN}. \quad \text{(A.6′)}$$

Put Eq. (A.3′) into Eq. (9)

$$\begin{aligned} F_{Kx}l_{IK}\frac{\sin(\theta_{IK}+\theta_{MO})}{\cos\theta_{MO}} &= F_{Ay}\left(l_{AC}\cos\theta_{AC} + l_{IC}\cos\theta_{IC}\right) \\ &+F_{Cx}\left(l_{IC}\sin\theta_{IC}\right) - F_{Cy}\left(l_{IC}\cos\theta_{IC}\right) + F_{Ex}\left(l_{IE}\sin\theta_{IE}\right) \\ &-F_{Ey}\left(l_{IE}\cos\theta_{IE}\right) + F_{Fx}\left(l_{IF}\sin\theta_{IF}\right) - F_{Fy}\left(l_{IF}\cos\theta_{IF}\right) \\ &+F_{Hx}\left(l_{IH}\sin\theta_{IH}\right) + F_{Hy}\left(l_{IH}\cos\theta_{IH}\right) - F_{Jx}\left(l_{IJ}\sin\theta_{IJ}\right) \quad \text{(A.9′)} \\ &+F_{Jy}\left(l_{IJ}\cos\theta_{IJ}\right) + F_{Mx}\left(\frac{l_{IK}l_{MO}}{l_{KO}}\frac{\cos\theta_{IK}\sin\theta_{MO}}{\cos\theta_{MO}}\right) \\ &+F_{My}\left(\frac{l_{IK}l_{MO}}{l_{KO}}\cos\theta_{IK}\right). \end{aligned}$$

Put Eqs. (A.3′) and (A.6′) into {Eq. (7) $\times\sin\theta_{LN}$ +Eq. (8) $\times\cos\theta_{LN}$}

$$\begin{aligned} F_{Kx}\frac{\sin(\theta_{MO}-\theta_{LN})}{\cos\theta_{MO}} &= -F_{Ay}\cos\theta_{LN} \\ &+\left(F_{Cx}\sin\theta_{LN} + F_{Cy}\cos\theta_{LN}\right) + \left(F_{Ex}\sin\theta_{LN} + F_{Ey}\cos\theta_{LN}\right) \\ &+\left(F_{Fx}\sin\theta_{LN} + F_{Fy}\cos\theta_{LN}\right) + \left(F_{Hx}\sin\theta_{LN} + F_{Hy}\cos\theta_{LN}\right) \\ &+\left(F_{Lx}\frac{l_{LN}}{l_{IN}}\sin\theta_{LN} + F_{Ly}\frac{l_{LN}}{l_{IN}}\cos\theta_{LN}\right) \quad \text{(A.10)} \\ &+\left(F_{Mx}\frac{l_{MO}}{l_{KO}}\frac{\sin\theta_{MO}\cos\theta_{LN}}{\cos\theta_{MO}} + F_{My}\frac{l_{MO}}{l_{KO}}\cos\theta_{LN}\right) \\ &+\left(F_{Jx}\sin\theta_{LN} + F_{Jy}\cos\theta_{LN}\right). \end{aligned}$$

F_{Kx} of Eq. (A.10) put into Eq. (A.9′), then the F_{Ay} calculated as below

$$\begin{aligned} F_{Ay} = \frac{1}{\Gamma}(&\Lambda_1 F_{Cx} + \Lambda_2 F_{Cy} + \Lambda_3 F_{Ex} + \Lambda_4 F_{Ey} + \Lambda_5 F_{Fx} + \Lambda_6 F_{Fy} \\ &+\Lambda_7 F_{Hx} + \Lambda_8 F_{Hy} + \Lambda_9 F_{Jx} + \Lambda_{10} F_{Jy} + \Lambda_{11} F_{Lx} + \Lambda_{12} F_{Ly} \quad \text{(A.11)} \\ &+\Lambda_{13} F_{Mx} + \Lambda_{14} F_{My}) \end{aligned}$$

where

$$\begin{aligned} \Gamma &= \left(l_{IK}\cos\theta_{LN}\right)\sin(\theta_{IK}+\theta_{MO}) \\ &+\left(l_{AC}\cos\theta_{AC} + l_{IC}\cos\theta_{IC}\right)\sin\left(\theta_{MO}-\theta_{LN}\right) \\ \Lambda_1 &= \left(l_{IK}\sin\theta_{LN}\right)\sin(\theta_{IK}+\theta_{MO}) - \left(l_{IC}\sin\theta_{IC}\right)\sin\left(\theta_{MO}-\theta_{LN}\right) \\ \Lambda_2 &= \left(l_{IK}\cos\theta_{LN}\right)\sin(\theta_{IK}+\theta_{MO}) + \left(l_{IC}\cos\theta_{IC}\right)\sin\left(\theta_{MO}-\theta_{LN}\right) \\ \Lambda_3 &= \left(l_{IK}\sin\theta_{LN}\right)\sin(\theta_{IK}+\theta_{MO}) - \left(l_{IE}\sin\theta_{IE}\right)\sin\left(\theta_{MO}-\theta_{LN}\right) \\ \Lambda_4 &= \left(l_{IK}\cos\theta_{LN}\right)\sin(\theta_{IK}+\theta_{MO}) + \left(l_{IE}\cos\theta_{IE}\right)\sin\left(\theta_{MO}-\theta_{LN}\right) \\ \Lambda_5 &= \left(l_{IK}\sin\theta_{LN}\right)\sin(\theta_{IK}+\theta_{MO}) - \left(l_{IF}\sin\theta_{IF}\right)\sin\left(\theta_{MO}-\theta_{LN}\right) \\ \Lambda_6 &= \left(l_{IK}\cos\theta_{LN}\right)\sin(\theta_{IK}+\theta_{MO}) + \left(l_{IF}\cos\theta_{IF}\right)\sin\left(\theta_{MO}-\theta_{LN}\right) \\ \Lambda_7 &= \left(l_{IK}\sin\theta_{LN}\right)\sin(\theta_{IK}+\theta_{MO}) - \left(l_{IH}\sin\theta_{IH}\right)\sin\left(\theta_{MO}-\theta_{LN}\right) \\ \Lambda_8 &= \left(l_{IK}\cos\theta_{LN}\right)\sin(\theta_{IK}+\theta_{MO}) - \left(l_{IH}\cos\theta_{IH}\right)\sin\left(\theta_{MO}-\theta_{LN}\right) \\ \Lambda_9 &= \left(l_{IK}\sin\theta_{LN}\right)\sin(\theta_{IK}+\theta_{MO}) + \left(l_{IJ}\sin\theta_{IJ}\right)\sin\left(\theta_{MO}-\theta_{LN}\right) \\ \Lambda_{10} &= \left(l_{IK}\cos\theta_{LN}\right)\sin(\theta_{IK}+\theta_{MO}) - \left(l_{IJ}\cos\theta_{IJ}\right)\sin\left(\theta_{MO}-\theta_{LN}\right) \\ \Lambda_{11} &= \left(\frac{l_{IK}l_{LN}}{l_{IN}}\sin\theta_{LN}\right)\sin(\theta_{IK}+\theta_{MO}) \\ \Lambda_{12} &= \left(\frac{l_{IK}l_{LN}}{l_{IN}}\cos\theta_{LN}\right)\sin(\theta_{IK}+\theta_{MO}) \\ \Lambda_{13} &= \left(\frac{l_{IK}l_{MO}}{l_{KO}}\right)\left(\frac{\sin\theta_{MO}}{\cos\theta_{MO}}\right) \\ &\quad \left\{\cos\theta_{LN}\sin(\theta_{IK}+\theta_{MO}) - \cos\theta_{IK}\sin\left(\theta_{MO}-\theta_{LN}\right)\right\} \\ \Lambda_{14} &= \left(\frac{l_{IK}l_{MO}}{l_{KO}}\right)\left\{\cos\theta_{LN}\sin(\theta_{IK}+\theta_{MO}) - \cos\theta_{IK}\sin\left(\theta_{MO}-\theta_{LN}\right)\right\}. \end{aligned}$$

Seung Joong Kim received his Ph.D. in Mechanical Engineering from KAIST. His research interests include turbulence, drag reduction and flow induced noise.

Hyeokbin Kwon is a Professor of the Department of Transportation System Engineering, Korea National University of Transportation, Uiwang, Gyeonggi-do, Korea. He received his Ph.D. in Aerospace Engineering from Seoul National University. His research interests include railway aerodynamics and future transportation system design.

Junsun Ahn is an Assistant Professor of the Ddepartment of Railway Vehicle System Engineering, Korea National University of Transportation, Uiwang, Gyeonggi-do, Korea. He received his Ph.D. in Mechanical Engineering from KAIST. His research interests include turbulence, flow control and railway aerodynamics.